Octahedral and tetrahedral coordination influences the ordering of oxygen vacancy channels in $SrCoO_{2.5}$ and $SrFeO_{2.5}$ thin films

Juan A. Santana,[1,2,3*] David Bugallo,[4] Andrew Mirea,[4] Tessa D. Tucker,[4] David Alfredo Gonzalez-Narvaez,[1] Alejandra Rosario-Crespo,[1] Yalexander Sanchez-Navarro,[1] Gabriela Marrero-Hernandez,[1,4] Kevin Rosa-Dieppa,[1,3] Andrea Garcia-Ramos,[1,3], Rajeev Kumar Rai,[5] Eric A. Stach,[5] Steven J. May,[4] Andrew M. Rappe[3]

[1]Department of Chemistry, University of Puerto Rico at Cayey, Cayey, PR 00737, USA
[2]Deanship of Academic Affairs, University of Puerto Rico at Cayey, Cayey, PR 00737, USA
[3] Department of Chemistry, University of Pennsylvania, Philadelphia, Pennsylvania 19104, USA
[4] Department of Materials Science and Engineering, Drexel University, Philadelphia, PA 19104, USA
[5]Department of Materials Science and Engineering, University of Pennsylvania, Pennsylvania 19104, USA

ABSTRACT.

In this study, we explore how the orientation of oxygen vacancy channels (OVCs) in $SrFeO_{2.5}$ and $SrCoO_{2.5}$ thin films is influenced by the metal-oxygen bonds in their octahedral and tetrahedral coordination environments. Using density-functional theory (DFT) calculations, we found that energy changes due to applied strain are driven primarily by the octahedral Fe-O bonds in $SrFeO_{2.5}$, leading to a strain-induced transition between perpendicular and parallel OVC relative to the substrate. In contrast, the tetrahedral Co-O bonds in $SrCoO_{2.5}$ primarily drive energy changes due to applied strain, resulting in a parallel OVC orientation regardless of the strain state. These computational findings are supported by experimental results obtained through molecular beam epitaxy (MBE) synthesis, x-ray diffraction (XRD) and scanning transmission electron microscopy (STEM) analysis. Our research underscores the critical role of metal-oxygen coordination environments in predicting and tailoring the properties of strained complex oxide thin films, providing a comprehensive understanding of the mechanisms governing vacancy ordering in brownmillerite structures.

1. Introduction

Substrate-induced strain is a widely used strategy to coax new or enhanced properties from materials in thin film form.[1–5] In cubic or pseudocubic crystal structures, such as zinc blende semiconductors or perovskite oxides, the responses to changes in lattice parameters typically exhibit straightforward trends in which tensile (compressive) in-plane strain within a film increases the in-plane (out-of-plane) parameters and contracts the out-of-plane (in-plane) parameters, which is accommodated through combinations of changes to bond lengths and angles.[6–9] In heteroepitaxial systems where the film crystal structure differs significantly from the substrate, epitaxial arrangements that minimize the symmetry and lattice mismatch and, therefore, reduce the elastic energy cost within the film are often observed. For example, perovskite oxides grown on Si can exhibit a 45° in-plane lattice rotation with respect to the substrate due to the approximate $\sqrt{2}:1$ ratio of lattice constants.[10,11] However, in the case of layered materials or compounds containing multiple distinct polyhedral units, the accuracy of using purely elastic or lattice mismatch-based arguments to predict epitaxial arrangements should not be taken as a given.

Epitaxial brownmillerite materials, with a composition of $A_2B_2O_5$, are prime candidates for studying how strain controls crystallographic orientation in complex materials. The brownmillerite structure can be portrayed as a perovskite crystal with a specific oxygen vacancy concentration and planar ordering, leading to alternating tetrahedral and octahedral coordination planes, enabling many valuable properties, including ionic conductivity,[12–14] memristive behavior,[15–17] robust magnetic ordering,[18,19] and multiferroicity or polarity.[20–22] Understanding the factors that influence the equilibrium structure of thin-film brownmillerite oxides is vital for customizing their functional properties, which are anisotropic and depend strongly on the ordering direction of the vacancy planes. Note that we will use the $ABO_{2.5}$ notation, which is commonly employed in the thin film community, to indicate the ordered brownmillerite structure, while in bulk materials, $A_2B_2O_5$ denotes brownmillerite and $ABO_{2.5}$ denotes a highly oxygen deficient perovskite without vacancy ordering.

Fe-based thin-film brownmillerites, such as $SrFeO_{2.5}$ and $CaFeO_{2.5}$, have been employed as model systems to investigate how strain can be used to control the orientation of vacancy ordering.[23,24] In a prominent study by Onoue and coauthors, brownmillerite $CaFeO_{2.5}$ thin films were deposited on $SrTiO_3$ (STO), $(La_{0.3}Sr_{0.7})(Al_{0.65}Ta_{0.35})O_3$ (LSAT), $LaAlO_3$ (LAO), and $LaSrAlO_4$ (LSAO) substrates using pulsed laser deposition.[25] X-ray diffraction was employed to show that the orientation of $CaFeO_{2.5}$ depends on the specific substrate. Under tensile strain induced from STO and LSAT substrates, $CaFeO_{2.5}$ exhibits alternately stacked layers of FeO_4 tetrahedra and FeO_6 octahedra parallel to the substrate plane, with the ordering vector of the oxygen vacancy channels (OVC) along the growth direction. Conversely, under compressive strain on LAO and LSAO, $CaFeO_{2.5}$ thin films have tetrahedral and octahedral layers perpendicular to the substrate plane, yielding an in-plane ordering vector of the OVCs.[25,26] This orientational behavior was also reported by Rossell and coauthors.[23] Due to the larger unit cell of $SrFeO_{2.5}$ compared to $CaFeO_{2.5}$, films of $SrFeO_{2.5}$ grown on LSAT and STO are under compressive strain and tend to exhibit an ordering vector in the plane of the film. Substrates with larger in-plane lattice constants, such as $GdScO_3$, are required to induce tensile strain into $SrFeO_{2.5}$ films. However, synthesis studies of $SrFeO_{2.5}$ films have also established that vacancy ordering can depend on specific growth conditions such as chamber pressure, temperature, electrolytic gating, and post-deposition annealing procedures.[27–31]

Less systematic research has been conducted to study the factors that control the orientation of strained alkaline earth Co-based brownmillerites. For instance, $SrCoO_{2.5}$ has been grown on

LAO(001),[32] LSAT(100),[33,34] LSAT(100), STO(100),[35–38] and yttria-stabilized zirconia (YSZ(001)).[39,40] These previous works report that $SrCoO_{2.5}$ has oxygen vacancy ordering parallel to the surface orientation on all these substrates. This observation contrasts with the findings for $CaFeO_{2.5}$ thin films and challenges the lattice mismatch hypothesis, where the orientation of OVC depends on the substrate-induced strain. Combining computational and experimental approaches, we also find strain-dependent vacancy ordering in $SrFeO_{2.5}$ and strain-independent vacancy ordering in $SrCoO_{2.5}$. We identify key features in the electronic structure and phonon density of states that we put forth as the origin of the difference in strain-dependent vacancy ordering in these two systems.

2. Methods

2.1. DFT calculations

We performed density-functional theory (DFT) calculations using the PBESol exchange-correlation functional and Hubbard U terms to correct the energies of the localized 3d orbitals. The projector augmented wave (PAW)[41] method was used to express the wave functions, as implemented in the Vienna Ab-initio Simulation Package (VASP).[42] We used $U_d = 5.0$ eV for Fe and $U_d = 3.0$ eV for Co. Calculations were also performed with other U_d values for Fe an Co, as well as using other DFT methods (see the Supporting Information Section) without significant changes in the results. We used O-, Sr-, Fe, and Co-PAW potentials with 6, 10, 16 and 17 valence electrons, respectively; these are the PAW_PBE-O, -Sr_sv, -Fe_sv, and -Co_sv POTCARs in the VASP distribution. A plane-wave cutoff energy of 500 eV was used to expand the valence portion of the wave functions, and a 4×2×4 k-point grid was used to sample the Brillouin zone.

The $SrFeO_{2.5}$ and $SrCoO_{2.5}$ brownmillerite thin films were simulated employing a 72-atom simulation cell, which is a 45° rotation of the *Pnma* phase of brownmillerite; see Figure S1 in the Supporting Information Section. The cubic (001) terminated perovskite substrate was simulated by fixing the $a = c = 2a_{\text{substrate}}$ lattice parameters in the plane with four layers along the growth direction for parallel OVC and $b = 4a_{\text{substrate}}$ and $c = 2a_{\text{substrate}}$ in the plane with two layers along the growth direction for perpendicular OVC, where $a_{\text{substrate}}$ is the bulk lattice parameter of each of the substrates. All calculations were performed for the G-type antiferromagnetic ordering.[43,44]

2.2. Molecular beam epitaxy

Thin films were grown by molecular beam epitaxy (MBE) inside an ultra-high vacuum chamber (base pressure ~ 10^{-9}-10^{-10} Torr).[45] Sr, Fe, and Co were evaporated independently from effusion cells, at temperatures of approximately 430°C, 1150°C, and 1350°C. This allows for a growth rate of ≈5 Å/min of the oxide material. The growth was done while introducing ultrapure oxygen gas into the chamber, at a pressure of 5×10^{-6} Torr, and while keeping the substrates at a nominal temperature of 600°C. Four different substrates were used at the same time to ensure that the thin film was synthesized under identical growth conditions at the different strain states.

2.3. Structural characterization

X-ray diffraction experiments were conducted on a Rigaku Smartlab or a Panalytical Empyrean. Out-of-plane 00*L* measurements were carried on both diffractometers, in high-resolution mode with a Ge double-bounce monochromator. In-plane measurements were performed on the Rigaku Smartlab, using the Ge double-bounce monochromator. Atomic-resolution high-angle annular dark-field (HAADF) -scanning transmission electron microscopy (STEM) was performed using aberration-corrected JEOL NEOARM operating at 200 kV. The HAADF-STEM images were acquired using 27 mrad convergence angle, 160 pA probe current and a camera length of 4 cm.

3. Results and discussion

3.1. Simulation of strained thin films of $SrFeO_{2.5}$ and $SrCoO_{2.5}$

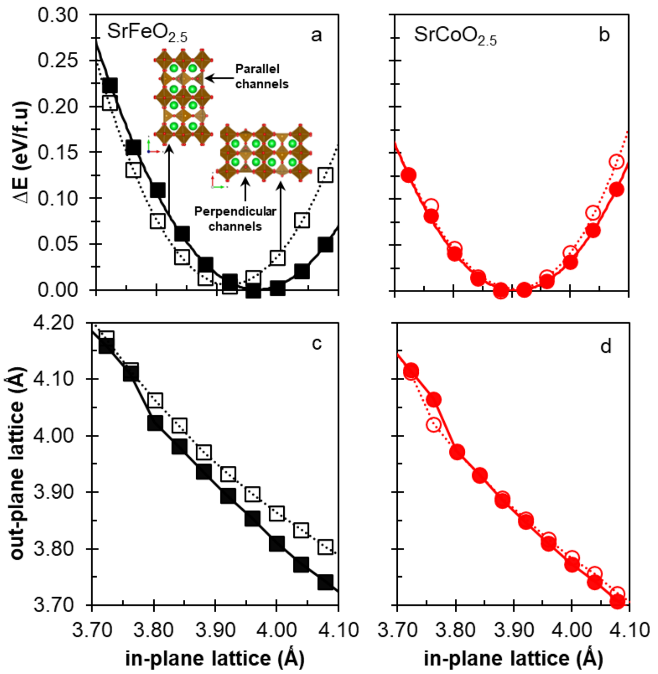

Figure 1. DFT calculated energy *vs*. imposed pseudocubic in-plane lattice parameter (parallel to the substrate surface) for unit cells of (a) $SrFeO_{2.5}$ and (b) $SrCoO_{2.5}$ with (filled symbols) parallel and (empty symbols) perpendicular OVCs relative to the substrate. Panels c and d display the out-of-plane lattice parameters (perpendicular to the substrate surface).

In **Figure 1a,b**, we present the DFT energy plotted against the in-plane lattice constant for thin films of $SrFeO_{2.5}$ and $SrCoO_{2.5}$, considering both parallel and perpendicular OVCs relative to the substrate. For $SrFeO_{2.5}$, we observe two stable structures: the perpendicular OVC is favored when the in-plane lattice constant is below 3.94 Å (under compressive strain), while the parallel OVC is favored for in-plane lattice constants above 3.94 Å (under tensile strain). In contrast, $SrCoO_{2.5}$ shows a single stable structure with the parallel OVC favored across all in-plane lattice constants. The difference in the structures of $SrFeO_{2.5}$ and $SrCoO_{2.5}$ can be observed in the calculated out-of-plane lattice parameters shown in **Figure 1c,d**, where $SrFeO_{2.5}$ displays two distinctive cell height parameters for parallel and perpendicular OVC, while $SrCoO_{2.5}$ has very similar cell heights for the two orientations. It is worth noting that similar trends are consistent with other DFT methods (see Figure S2 in the Supporting Information Section).

Our calculated findings for $SrFeO_{2.5}$ and $SrCoO_{2.5}$ are intriguing. The results for $SrFeO_{2.5}$ align closely with expectations based on lattice mismatches between the film and substrate.[25] For the brownmillerite $Sr_2Fe_2O_5$, the pseudocubic lattice parameters are slightly smaller along the ordering vector ($b_p = 3.90$ Å)[44,46] than they are within the planes of vacancies ($a_p = 3.91$ Å).[44,46] Therefore, one would expect compressive strain to lead to perpendicular OVC and tensile strain to lead to parallel OVC as observed in Figure 1a. A similar lattice mismatch argument for $SrCoO_{2.5}$ ($a_p = 3.86$ Å and $b_p = 3.91$ Å)[43] would predict a transition from parallel to perpendicular OVC with opposite strain dependence to the ferrites because $a_p < b_p$. However, such a transition is not present in our DFT results (Figure 1b).

A model based on the electrostatic and elastic considerations of thin-film brownmillerite oxides that goes beyond lattice mismatches was recently developed based on DFT calculations and applied to ferrite brownmillerites.[47] According to this model,[47] the distinct structures (perpendicular vs. parallel) observed at different in-plane strain conditions come from i) a change in the separation within the tetrahedral chains relative to the octahedra and ii) the octahedral distortion. For $SrFeO_{2.5}$, such transition takes place when the substrate in-plane lattice value reaches 3.92 Å (refer to Figure S3 in the Supporting Information Section). In-plane lattice values below 3.92 Å make the parallel OVC in $SrFeO_{2.5}$ energetically unfavorable as compare to the perpendicular OVC, due to the reduce separation within the tetrahedral chains (increasing electrostatic repulsion) and increased octahedral distortion (increasing elastic strain energy).[47] When the in-plane lattice values exceed 3.92 Å, the parallel OVC in $SrFeO_{2.5}$ become energetically favorable. Similar electrostatic and elastic considerations applied to $SrCoO_{2.5}$ would anticipate a transition from perpendicular to parallel OVC when the in-plane lattice value exceeds 3.87 Å (refer to Figure S3 in the Supporting Information Section). However, the DFT energy *vs*. in-plane lattice constant for strained $SrCoO_{2.5}$ (Figure 1b) displays no transition.

3.2. Synthesis and characterization of thin films of $SrFeO_{2.5}$ and $SrCoO_{2.5}$

To test the validity of the calculations, we synthesized $SrFeO_{2.5}$ and $SrCoO_{2.5}$ films on LAO (001) ($a_p = 3.795$ Å), LSAT (001) ($a_p = 3.870$ Å), STO (001) ($a_p = 3.905$ Å) and $GdScO_3$ (GSO) (001) ($a_p = 3.964$ Å). The use of MBE provides a synthetic approach that is closer to equilibrium than pulsed laser deposition or sputtering, which utilize higher kinetic energy processes to deposit the films. Thus, while the DFT calculations capture a 0 K equilibrium state, MBE may provide the closest agreement out of available physical vapor deposition techniques. In the following discussion, we define the *c*-axis of films as the out-of-plane (growth) axis.

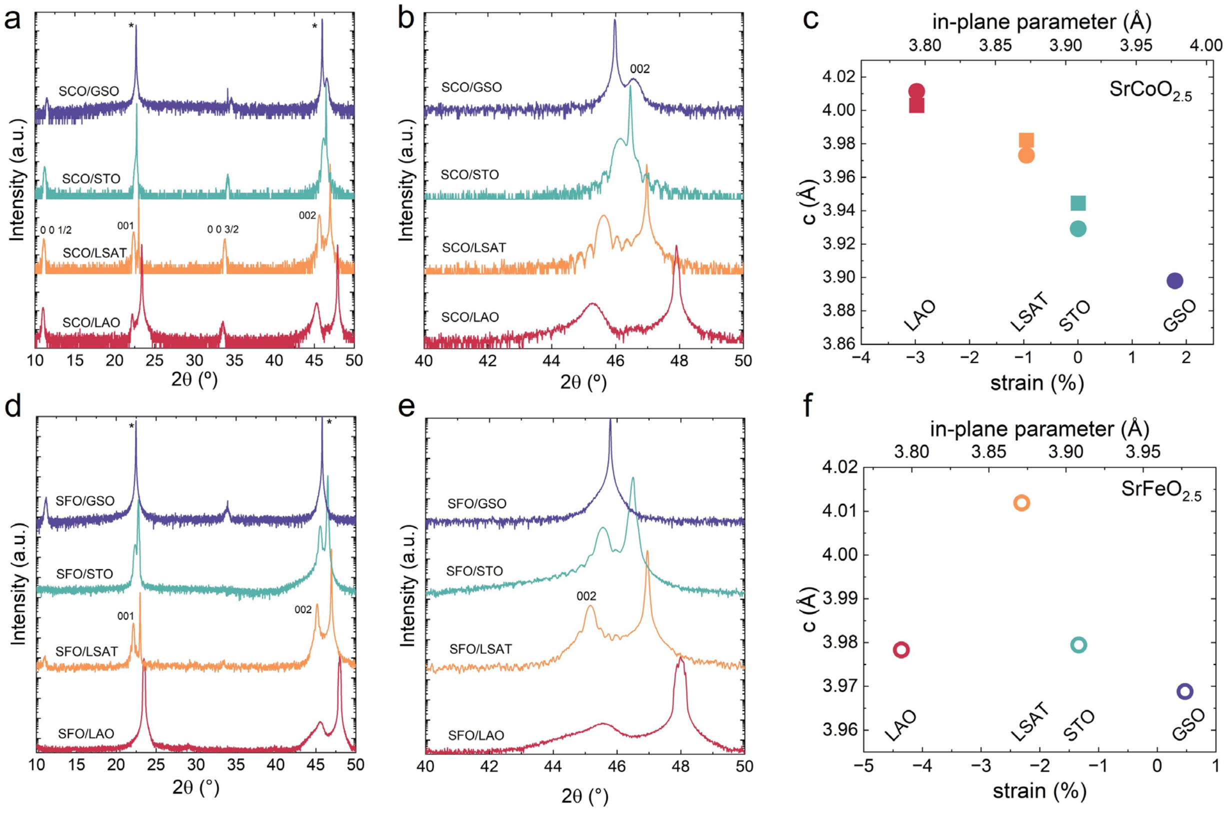

Figure 2. XRD data for $SrCoO_{2.5}$ and $SrFeO_{2.5}$ on different substrates. 2θ/ω scans for (a,b) $SrCoO_{2.5}$ films and (d,e) $SrFeO_{2.5}$ films on different substrates. The substrate peaks are the sharp, intense peaks marked by the * for GSO. The pseudocubic out-of-plane pseudocubic lattice parameters obtained from x-ray diffraction for (c) $SrCoO_{2.5}$ and (f) $SrFeO_{2.5}$, respectively, as a function of the lattice mismatch with the substrate. Circles in c) correspond to the data from samples in a) and b), while squares correspond to a different growth set. All peak indexing for the films is relative to the pseudocubic perovskite unit cell.

Specular X-ray diffractograms (Figure 2) show that $SrCoO_{2.5}$ films for all strain states exhibit half-order peaks along the 00*L* direction, while only positive strain states (in-plane lattice > 3.95 Å) produce this ordering for $SrFeO_{2.5}$. These half-order peaks, relative to the pseudocubic lattice, arise from ordering of the oxygen vacancy planes parallel to the (001) growth plane of the substrate and the accompanying *A*-site displacements along the ordering direction.[25] The vacancy ordering and *A*-site displacements double the pseudocubic unit cell along the ordering direction. Therefore, the presence of 0 0 $n/2$ half-order peaks (n = integer) are the direct experimental signature of parallel OVCs where the ordering direction is [001] (along the growth direction). The X-ray results agree with the DFT calculations in **Figure 1** showing that the cobaltite system presents parallel vacancy ordering under all strain states, while the ferrite system experiences a transition from perpendicular ordering under compressive strain to parallel ordering at tensile strain. It is also worth mentioning that the $SrFeO_{2.5}$ sample grown on LAO is not coherently strained to the substrate, as apparent from its deviation from the trend of *c*-axis parameter as a function of the lattice mismatch [red circle in Fig. 2(f)]. The diffraction peak from this film has two components, a main peak from the relaxed component and a broad feature at lower angles likely arising from a thin strained layer.

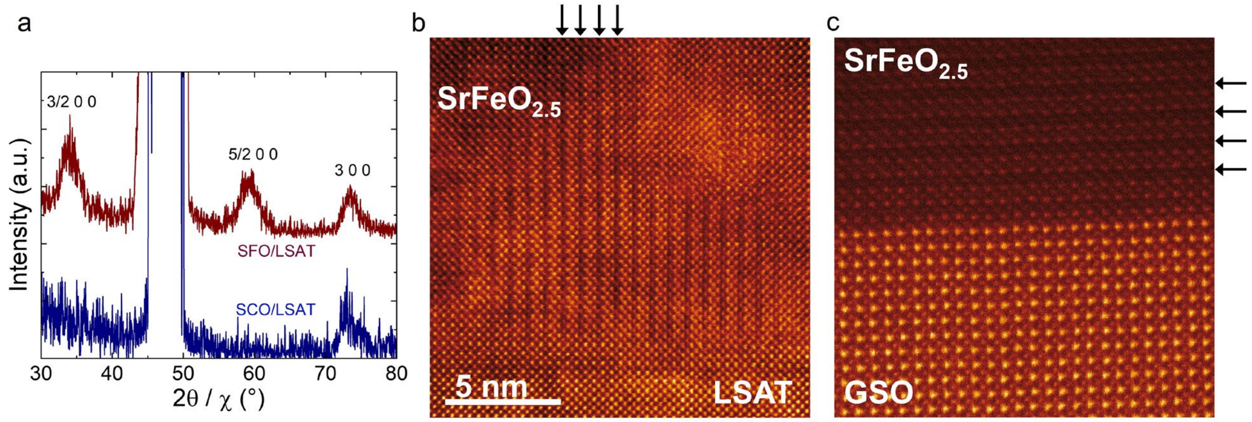

Figure 3. (a) *H*00 diffractograms of $SrCoO_{2.5}$ and $SrFeO_{2.5}$ thin films on LSAT substrates. $SrFeO_{2.5}$ presents a half-order peaks in the *H*00 scan, around 35 and 60 degrees, which are absent in $SrCoO_{2.5}$. Images obtained from scanning transmission electron microscopy of (b) a $SrFeO_{2.5}$ film on LSAT and (c) a $SrFeO_{2.5}$ film on $GdScO_3$. Perpendicular ordering of oxygen vacancies is present in SFO/LSAT, which are highlighted by the black arrows. Parallel ordering of oxygen vacancies is apparent in SFO/GSO due to the tensile strain and are highlighted by the black arrows.

To confirm the strain-induced transition from perpendicular to parallel OCV ordering in $SrFeO_{2.5}$, in-plane XRD and scanning transmission electron microscopy were performed. The in-plane XRD scans (**Figure 3**a) show half-order peaks along the *H*00 direction for a $SrFeO_{2.5}$ sample grown on LSAT substrate, while these peaks are absent for $SrCoO_{2.5}$ on LSAT. Scanning transmission electron microscopy provides real space imaging of the vacancy planes, in agreement with the x-ray diffraction results. Perpendicular ordering is apparent in the $SrFeO_{2.5}$ on LSAT [Fig. 3(b)] while parallel ordering of vacancy planes is clearly visible in $SrFeO_{2.5}$ on $GdScO_3$ [Fig. 3(c)].

3.3. Octahedral and tetrahedral coordination influences the ordering of OVCs in $SrCoO_{2.5}$ and $SrFeO_{2.5}$ thin films

Here we suggest that the key to understanding the orientation of OVC in brownmillerite thin films lies in examining the relative stiffness of the metal-oxygen tetrahedral and octahedral bonds within these materials. In brownmillerite thin films like $SrFeO_{2.5}$ and $SrCoO_{2.5}$, there are multiple coordination environments (more than one type of bonding geometry between the transition metal-oxygen). Our hypothesis is that when a given amount of strain is applied the stiffer bond results in a larger energy change as compared to a softer bond (**Figure 4**a), and therefore, the stiffer bond type in a brownmillerite thin films determines the preferred orientation of its OVC.

Specifically, our hypothesis suggests that in brownmillerites with either parallel or perpendicular OVCs, the energy changes due to applied strain should be similar for both OVCs orientation if these changes are driven mainly by sites with tetrahedral coordination (T_h), where oxygen atoms form a tetrahedral geometry around the metal center (if bonds in T_h sites are stiffer than other). As shown schematically in **Figure 4**b, bonding in tetrahedral coordination T_h sites in brownmillerites lies between axes, allowing T_h-site bonding to adjust similarly to the applied strain in both OVCs orientation (**Figure 4**d,f), resulting in similar energy changes for both OVCs orientation.

Conversely, if energy changes due to applied strain are driven mainly by sites in octahedral coordination (O_h), where oxygen atoms form an octahedral geometry around the metal center (if bonds in O_h sites are stiffer than other), which are axis-aligned bonding, the energy changes should be different for parallel and perpendicular OVCs. This is because O_h sites in brownmillerite thin films like $SrFeO_{2.5}$ and $SrCoO_{2.5}$ are not symmetric due to octahedral distortion, with two different types of bonds, one elongated along one direction and two similar along the two other directions. As a result, the geometry (**Figure 4**c,e) and energy changes driven by O_h sites depend on OVCs orientation.

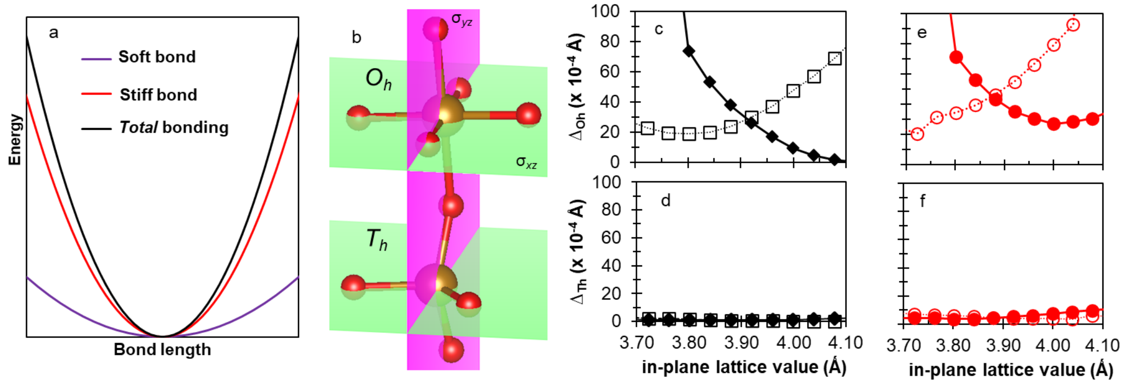

Figure 4. Panel (a) shows a schematic of a hypothetical system with soft and stiff bonding, where stiff bonding contributes more to energy changes due to imposed strain. Panel (b) shows a schematic of the octahedral and tetrahedral coordination: O_h bonding are along the axis, and T_h bonding are in the planes. Panels c, d, e and f show the DFT calculated (c, e) distortion Δ_{Oh} of the octahedra and (d, f) distortion Δ_{Th} of the tetrahedra in (c, d) $\mathrm{SrFeO_{2.5}}$ and (e, f) $\mathrm{SrCoO_{2.5}}$; filled and empty symbols are parallel and perpendicular OVCs, respectively.

In the case of $\mathrm{SrCoO_{2.5}}$, our calculations suggest that there is no transition from parallel to perpendicular ordering because the energy change due to applied strain is driven mainly by Co in tetrahedral coordination (Co_{Th}) (stiffer bonds in $\mathrm{SrCoO_{2.5}}$). As shown schematically in **Figure 4**b, bonding in T_h sites lies between the axes, allowing Co_{Th} bonding to adjust to the applied strain, resulting in small geometry changes (**Figure 4**d). In other words, when strain is applied to $\mathrm{SrCoO_{2.5}}$ with either parallel or perpendicular OVCs, the energy changes driven by Co_{Th} is similar for both orientations. In the case of $\mathrm{SrFeO_{2.5}}$, our model suggests that the energy change due to applied strain is larger in the Fe in octahedral coordination (Fe_{Oh}), which are axis-aligned bonding, compared to the tetrahedral Fe (Fe_{Th}). This results in different geometry (**Figure 4**c) and energy changes for parallel and perpendicular OVCs.

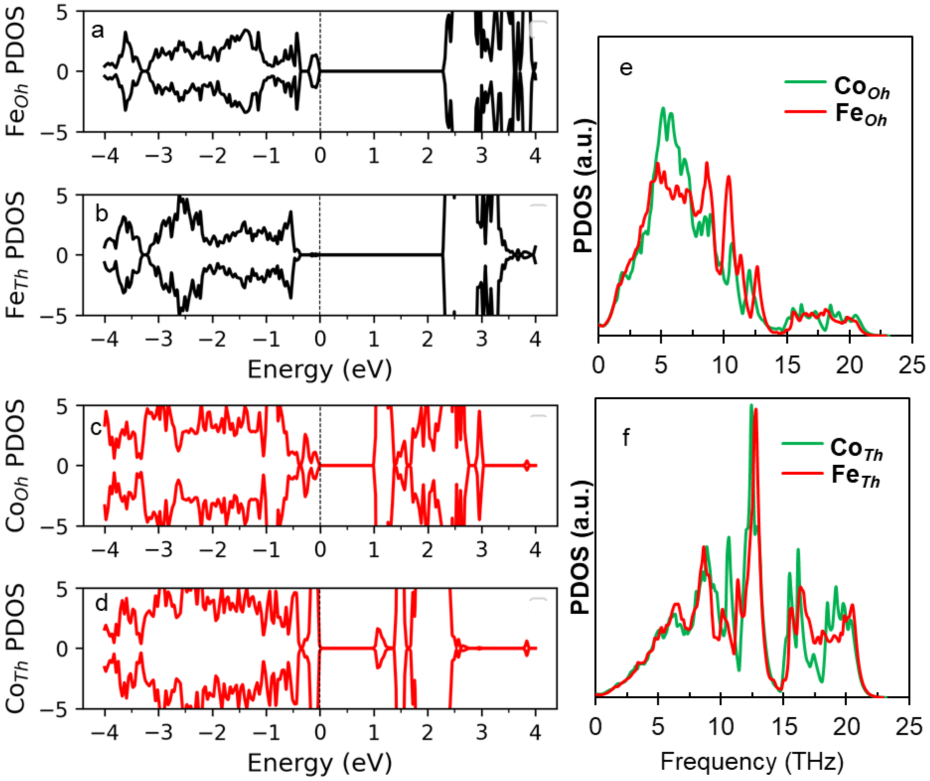

Figure 5. DFT calculated partial density of states (PDOS) for (a) Fe ions in octahedral coordination (Fe$_{Oh}$), and (b) tetrahedral coordination (Fe$_{Th}$) in SrFeO$_{2.5}$, (c) Co ions in octahedral coordination (Co$_{Oh}$) and (d) tetrahedral coordination (Co$_{Th}$) in SrCoO$_{2.5}$ with parallel OVC and $a_{\text{substrate}}$ = 3.96 Å. Phonon PDOS are presented for (e) Fe$_{Oh}$ and Co$_{Oh}$ and (f) Fe$_{Th}$ and Co$_{Th}$.

To provide computational support for our model, we analyzed both the electronic and phonon PDOS to explore the bonding characteristics in SrFeO$_{2.5}$ and SrCoO$_{2.5}$. The phonon PDOS directly reflects bond stiffness through vibrational frequencies, with stiffer bonds exhibiting higher phonon frequencies. The electronic PDOS, on the other hand, offers complementary insights into bonding by revealing the contributions of various atomic orbitals to the electronic structure, particularly near the valence band maximum (VBM). This helps identify which atomic sites and bonding environments influence the states near the VBM, offering a deeper understanding of the electronic behavior of the material in conjunction with the mechanical insights from the phonon analysis.

Our DFT calculations indicate that the VBM is associated with Fe in octahedral coordination (Fe_{Oh}) in $SrFeO_{2.5}$ (Figure 5a). The corresponding PDOS for Fe in the tetrahedral coordination (Fe_{Th}) does not show similar features near the VBM (Figure 5b), but instead these Fe_{Th} derived states appear ~0.5 eV below the VBM. On the other hand, calculations show that the VBM of $SrCoO_{2.5}$ is highly associated with Co ions in tetrahedral coordination (Co_{Th}) (see Figure 5c,d). These results suggest that the electronic properties of $SrFeO_{2.5}$ and $SrCoO_{2.5}$ are strongly influenced by the coordination geometry of the metal ions (Fe and Co). The coordination environment (octahedral vs. tetrahedral) significantly affects where the electronic states appear in the band structure.

Figure 5e presents our DFT results for the phonon PDOS of Fe_{Oh} and Co_{Oh} in $SrFeO_{2.5}$ and $SrCoO_{2.5}$. The results show that Fe_{Oh} in $SrFeO_{2.5}$ has higher phonon frequencies than Co_{Oh} in $SrCoO_{2.5}$. In the case of Fe_{Th} and Co_{Th}, phonon frequencies are rather similar, with Co_{Th} having a slightly higher PDOS at high frequencies. These results for phonon PDOS indicate that the bonding for Fe_{Oh} in $SrFeO_{2.5}$ is stiffer than Co_{Oh} in $SrCoO_{2.5}$.

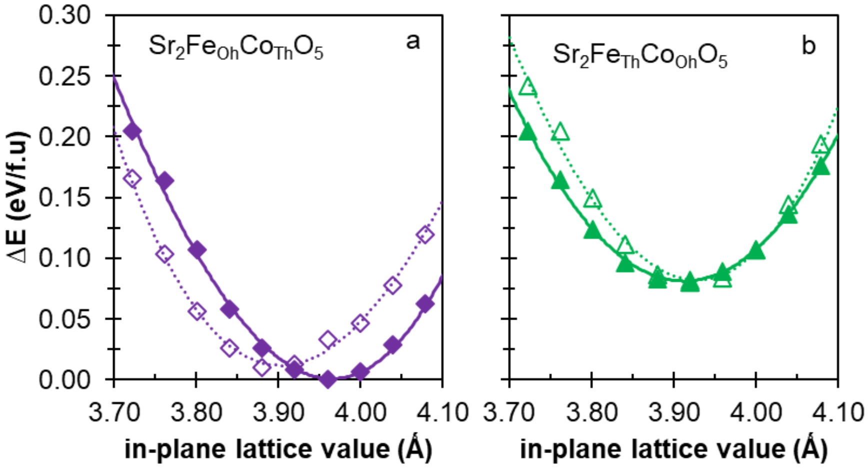

Figure 6. DFT calculated energy *vs*. imposed pseudocubic in-plane lattice parameter for unit cells of (a) $Sr_2Fe_{Oh}Co_{Th}O_5$ and (b) $Sr_2Fe_{Th}Co_{Oh}O_{2.5}$ with (filled symbols) parallel and (empty symbols) perpendicular OVCs.

Another computational alternative to show the effect of coordination in the orientation of OVCs is to consider the fact that the chemical bond in dimer Fe-O[48] is stronger and stiffer[49,50] than in Co-O.[51] In calculations performed for Sr_2FeCoO_5 (or $SrFe_{0.5}Co_{0.5}O_{2.5}$) we can computationally specify the location of Fe and Co in either octahedral or tetrahedral coordination. Since Fe-O in this material is expected to be the stronger and stiffer bond, we can explore the effects of coordination on the orientation of OVCs directly. We show in **Figure 6** results for such simulations. As expected from our model, when the stiffer bond is on the octahedral coordination sites, as is the case for $Sr_2Fe_{Oh}Co_{Th}O_5$, a strain-driven transition between two orientations is observed. If the stiffer bond is on the tetrahedral coordination sites, as is the case of $Sr_2Fe_{Th}Co_{Oh}O_5$, the parallel OVC orientation is dominant for all lattice constants, consistent with what we observe experimentally in $SrCoO_{2.5}$ films.

4. Conclusion

Our investigation into the orientation of oxygen vacancy channels (OVCs) in $SrFeO_{2.5}$ and $SrCoO_{2.5}$ thin films reveals critical insights into the role of metal-oxygen coordination environments. By combining density-functional theory (DFT) calculations with experimental techniques, we have demonstrated that the octahedral and tetrahedral coordination environments significantly influence the ordering of OVCs under strain. The distinct responses of $SrFeO_{2.5}$ and $SrCoO_{2.5}$ to applied strain suggest that tuning metal-oxygen bond characteristics is an effective strategy for controlling OVC orientation in various brownmillerites, including alloy variants. By systematically varying metal cation ratios and strained states, researchers can tailor brownmillerite properties to meet specific application requirements, such as enhanced ionic conductivity, tailored magnetic properties, or controlled memristive behavior. Our research underscores the importance of understanding coordination chemistry in brownmillerite structures and provides a robust framework for designing advanced materials with controlled ion migration pathways, contributing to the development of next-generation functional materials for diverse technological applications.

ASSOCIATED CONTENT

Supporting Information. Sketch of the model of brownmillerite; results of additional DFT calculations. This material is available free of charge via the Internet at http://pubs.acs.org.

AUTHOR INFORMATION

Corresponding Authors

Juan A. Santana: juan.santana6@upr.edu

Author Contributions

J.A.S., A.M.R, S.J.M and E.A.S conceptualize the project. J. A. S. directed the computational research, in coordination with A. M. R. Calculations, visualization, and analysis were performed by D.G., A.R., Y.S., G.M.H., K.R.D., A.G. and J.A.S. Thin film growth and X-ray characterization were performed by D.B., A. M., T. D.T, G.M.H, and S.J.M. Scanning transmission electron microscopy (STEM) measurements were performed by R.K.R and E.A.S. The manuscript was written through contributions of all authors. All authors have approved the final version of the manuscript.

Notes

The authors declare no competing financial interest.

ACKNOWLEDGMENTS

The work of J.A.S., D.G., A.R., Y.S., G.M.H., K.R.D and A.G. were supported by the National Science Foundation, through the Partnerships for Research and Education in Materials Research (PREM) program, under grant NSF-DMR-2122-102. A.M.R. acknowledges the support of the Army Research Laboratory via the Collaborative for Hierarchical Agile and Responsive Materials (CHARM) under cooperative agreement W911-NF-19-2-0119. Y.S., K.R.D and A.G. were partly supported by the National Science Foundation under Grant No. CHE-2001611, the NSF Center for Sustainable Nanotechnology (CSN). D.G. and A.R. were partly supported by the National Institute of General Medical Sciences of the National Institutes of Health under Award Number

T34GM145404. D.B. acknowledges the funding received from the European Union through the Marie Skłodowska-Curie Actions Postdoctoral Fellowship (ref. 101063432). T.D.T and S.J.M. were partly supported by the National Science Foundation, under grant number CMMI-2001888. Calculations were performed on the computing facility of the Laboratory of Modeling, Simulations, and Theory at the University of Puerto Rico at Cayey, which is supported in part by the National Institute of General Medical Sciences of the National Institutes of Health through Grant NIH NIGMS/INBRE P20GM103475, NASA-EPSCoR Grant 80NSSC21M0328 and the Puerto Rico Science, Technology & Research Trust Grant 9450864. The content is solely the responsibility of the authors and does not necessarily represent the official views of the National Institutes of Health.

REFERENCES

(1) Mii, Y. J.; Xie, Y. H.; Fitzgerald, E. A.; Monroe, D.; Thiel, F. A.; Weir, B. E.; Feldman, L. C. Extremely High Electron Mobility in Si/GexSi1−x Structures Grown by Molecular Beam Epitaxy. *Appl. Phys. Lett.* **1991**, *59* (13), 1611–1613. https://doi.org/10.1063/1.106246.

(2) Haeni, J. H.; Irvin, P.; Chang, W.; Uecker, R.; Reiche, P.; Li, Y. L.; Choudhury, S.; Tian, W.; Hawley, M. E.; Craigo, B.; Tagantsev, A. K.; Pan, X. Q.; Streiffer, S. K.; Chen, L. Q.; Kirchoefer, S. W.; Levy, J.; Schlom, D. G. Room-Temperature Ferroelectricity in Strained SrTiO3. *Nature* **2004**, *430* (7001), 758–761. https://doi.org/10.1038/nature02773.

(3) Brüne, C.; Liu, C. X.; Novik, E. G.; Hankiewicz, E. M.; Buhmann, H.; Chen, Y. L.; Qi, X. L.; Shen, Z. X.; Zhang, S. C.; Molenkamp, L. W. Quantum Hall Effect from the Topological Surface States of Strained Bulk HgTe. *Phys. Rev. Lett.* **2011**, *106* (12), 126803. https://doi.org/10.1103/PhysRevLett.106.126803.

(4) Yildiz, B. “Stretching” the Energy Landscape of Oxides—Effects on Electrocatalysis and Diffusion. *MRS Bull.* **2014**, *39* (2), 147–156. https://doi.org/10.1557/mrs.2014.8.

(5) Naumis, G. G.; Barraza-Lopez, S.; Oliva-Leyva, M.; Terrones, H. Electronic and Optical Properties of Strained Graphene and Other Strained 2D Materials: A Review. *Rep. Prog. Phys.* **2017**, *80* (9), 096501. https://doi.org/10.1088/1361-6633/aa74ef.

(6) Sun, Y.; Thompson, S. E.; Nishida, T. Physics of Strain Effects in Semiconductors and Metal-Oxide-Semiconductor Field-Effect Transistors. *J. Appl. Phys.* **2007**, *101* (10), 104503. https://doi.org/10.1063/1.2730561.

(7) Schlom, D. G.; Chen, L.-Q.; Fennie, C. J.; Gopalan, V.; Muller, D. A.; Pan, X.; Ramesh, R.; Uecker, R. Elastic Strain Engineering of Ferroic Oxides. *MRS Bull.* **2014**, *39* (2), 118–130. https://doi.org/10.1557/mrs.2014.1.

(8) Rondinelli, J. M.; May, S. J.; Freeland, J. W. Control of Octahedral Connectivity in Perovskite Oxide Heterostructures: An Emerging Route to Multifunctional Materials Discovery. *MRS Bull.* **2012**, *37* (3), 261–270. https://doi.org/10.1557/mrs.2012.49.

(9) Sando, D. Strain and Orientation Engineering in ABO3 Perovskite Oxide Thin Films. *J. Phys. Condens. Matter* **2022**, *34* (15), 153001. https://doi.org/10.1088/1361-648X/ac4c61.

(10) McKee, R. A.; Walker, F. J.; Chisholm, M. F. Crystalline Oxides on Silicon: The First Five Monolayers. *Phys. Rev. Lett.* **1998**, *81* (14), 3014–3017. https://doi.org/10.1103/PhysRevLett.81.3014.

(11) Baek, S.-H.; Eom, C.-B. Epitaxial Integration of Perovskite-Based Multifunctional Oxides on Silicon. *Acta Mater.* **2013**, *61* (8), 2734–2750. https://doi.org/10.1016/j.actamat.2012.09.073.

(12) Zhang, G. B.; Smyth, D. M. Defects and Transport of the Brownmillerite Oxides with High Oxygen Ion Conductivity — Ba2In2O5. *Solid State Ion.* **1995**, *82* (3), 161–172. https://doi.org/10.1016/0167-2738(95)00196-2.

(13) Lu, N.; Zhang, Z.; Wang, Y.; Li, H.-B.; Qiao, S.; Zhao, B.; He, Q.; Lu, S.; Li, C.; Wu, Y.; Zhu, M.; Lyu, X.; Chen, X.; Li, Z.; Wang, M.; Zhang, J.; Tsang, S. C.; Guo, J.; Yang, S.; Zhang, J.; Deng, K.; Zhang, D.; Ma, J.; Ren, J.; Wu, Y.; Zhu, J.; Zhou, S.; Tokura, Y.; Nan, C.-W.; Wu, J.; Yu, P. Enhanced Low-Temperature Proton Conductivity in Hydrogen-Intercalated Brownmillerite Oxide. *Nat. Energy* **2022**, *7* (12), 1208–1216. https://doi.org/10.1038/s41560-022-01166-8.

(14) Auckett, J. E.; Studer, A. J.; Pellegrini, E.; Ollivier, J.; Johnson, M. R.; Schober, H.; Miiller, W.; Ling, C. D. Combined Experimental and Computational Study of Oxide Ion Conduction

Dynamics in Sr2Fe2O5 Brownmillerite. *Chem. Mater.* **2013**, *25* (15), 3080–3087. https://doi.org/10.1021/cm401278m.

(15) Nallagatla, V. R.; Heisig, T.; Baeumer, C.; Feyer, V.; Jugovac, M.; Zamborlini, G.; Schneider, C. M.; Waser, R.; Kim, M.; Jung, C. U.; Dittmann, R. Topotactic Phase Transition Driving Memristive Behavior. *Adv. Mater.* **2019**, *31* (40), 1903391. https://doi.org/10.1002/adma.201903391.

(16) Tian, J.; Wu, H.; Fan, Z.; Zhang, Y.; Pennycook, S. J.; Zheng, D.; Tan, Z.; Guo, H.; Yu, P.; Lu, X.; Zhou, G.; Gao, X.; Liu, J.-M. Nanoscale Topotactic Phase Transformation in SrFeOx Epitaxial Thin Films for High-Density Resistive Switching Memory. *Adv. Mater.* **2019**, *31* (49), 1903679. https://doi.org/10.1002/adma.201903679.

(17) Saleem, M. S.; Cui, B.; Song, C.; Sun, Y.; Gu, Y.; Zhang, R.; Fayaz, M. U.; Zhou, X.; Werner, P.; Parkin, S. S. P.; Pan, F. Electric Field Control of Phase Transition and Tunable Resistive Switching in SrFeO2.5. *ACS Appl. Mater. Interfaces* **2019**, *11* (6), 6581–6588. https://doi.org/10.1021/acsami.8b18251.

(18) Schmidt, M.; Campbell, S. Crystal and Magnetic Structures of Sr 2Fe 2O 5 at Elevated Temperature. *J. Solid State Chem. - J SOLID STATE CHEM* **2001**, *156*, 292–304. https://doi.org/10.1006/jssc.2000.8998.

(19) Sullivan, E.; Hadermann, J.; Greaves, C. Crystallographic and Magnetic Characterisation of the Brownmillerite Sr2Co2O5. *J. Solid State Chem.* **2011**, *184* (3), 649–654. https://doi.org/10.1016/j.jssc.2011.01.026.

(20) Abe, N.; Khanh, N. D.; Sasaki, T.; Arima, T. Magnetic-Field-Induced Spin Flop Transition and Magnetoelectric Effect in Ca2Fe2-xAlxO5. *Phys. Rev. B* **2014**, *89* (5), 054437. https://doi.org/10.1103/PhysRevB.89.054437.

(21) Young, J.; Moon, E. J.; Mukherjee, D.; Stone, G.; Gopalan, V.; Alem, N.; May, S. J.; Rondinelli, J. M. Polar Oxides without Inversion Symmetry through Vacancy and Chemical Order. *J. Am. Chem. Soc.* **2017**, *139* (7), 2833–2841. https://doi.org/10.1021/jacs.6b10697.

(22) Kang, K. T.; Roh, C. J.; Lim, J.; Min, T.; Lee, J. H.; Lee, K.; Lee, T. Y.; Kang, S.; Seol, D.; Kim, J.; Ohta, H.; Khare, A.; Park, S.; Kim, Y.; Chae, S. C.; Oh, Y. S.; Lee, J.; Yu, J.; Lee, J. S.; Choi, W. S. A Room-Temperature Ferroelectric Ferromagnet in a 1D Tetrahedral Chain Network. *Adv. Mater.* **2019**, *31* (24), 1808104. https://doi.org/10.1002/adma.201808104.

(23) Rossell, M. D.; Lebedev, O. I.; Van Tendeloo, G.; Hayashi, N.; Terashima, T.; Takano, M. Structure of Epitaxial Ca2Fe2O5 Films Deposited on Different Perovskite-Type Substrates. *J. Appl. Phys.* **2004**, *95* (9), 5145–5152. https://doi.org/10.1063/1.1689003.

(24) Yan, F.; Wu, J.; Ning, S.; Luo, F. Orienting Oxygen Vacancy Channels in Brownmillerite Strontium Ferrite Thin Films Using Strain: Implications for Facile Oxygen Ion Transport. *ACS Appl. Nano Mater.* **2024**, *7* (7), 7703–7708. https://doi.org/10.1021/acsanm.4c00356.

(25) Inoue, S.; Kawai, M.; Ichikawa, N.; Kageyama, H.; Paulus, W.; Shimakawa, Y. Anisotropic Oxygen Diffusion at Low Temperature in Perovskite-Structure Iron Oxides. *Nat. Chem.* **2010**, *2* (3), 213–217. https://doi.org/10.1038/nchem.547.

(26) Lim, J. S.; Lee, J.; Lee, B. J.; Kim, Y.-J.; Park, H.-S.; Suh, J.; Nahm, H.-H.; Kim, S.-W.; Cho, B.-G.; Koo, T. Y.; Choi, E.; Kim, Y.-H.; Yang, C.-H. Harnessing the Topotactic Transition in Oxide Heterostructures for Fast and High-Efficiency Electrochromic Applications. *Sci. Adv.* **2020**, *6* (41), eabb8553. https://doi.org/10.1126/sciadv.abb8553.

(27) Saleem, M. S.; Song, C.; Gu, Y.; Chen, R.; Fayaz, M. U.; Hao, Y.; Pan, F. Orientation Control of Oxygen Vacancy Channels in Brownmillerite SrFeO2.5. *Phys. Rev. Mater.* **2020**, *4* (1), 014403. https://doi.org/10.1103/PhysRevMaterials.4.014403.

(28) Wang, L.; Yang, Z.; Bowden, M. E.; Du, Y. Brownmillerite Phase Formation and Evolution in Epitaxial Strontium Ferrite Heterostructures. *Appl. Phys. Lett.* **2019**, *114* (23), 231602. https://doi.org/10.1063/1.5096769.

(29) Han, H.; Sharma, A.; Meyerheim, H. L.; Yoon, J.; Deniz, H.; Jeon, K.-R.; Sharma, A. K.; Mohseni, K.; Guillemard, C.; Valvidares, M.; Gargiani, P.; Parkin, S. S. P. Control of Oxygen Vacancy Ordering in Brownmillerite Thin Films via Ionic Liquid Gating. *ACS Nano* **2022**, *16* (4), 6206–6214. https://doi.org/10.1021/acsnano.2c00012.

(30) Khare, A.; Lee, J.; Park, J.; Kim, G.-Y.; Choi, S.-Y.; Katase, T.; Roh, S.; Yoo, T. S.; Hwang, J.; Ohta, H.; Son, J.; Choi, W. S. Directing Oxygen Vacancy Channels in SrFeO2.5 Epitaxial Thin Films. *ACS Appl. Mater. Interfaces* **2018**, *10* (5), 4831–4837. https://doi.org/10.1021/acsami.7b17377.

(31) Roh, S.; Lee, S.; Lee, M.; Seo, Y.-S.; Khare, A.; Yoo, T.; Woo, S.; Choi, W. S.; Hwang, J.; Glamazda, A.; Choi, K.-Y. Oxygen Vacancy Induced Structural Evolution of SrFeO3-Epitaxial Thin Film from Brownmillerite to Perovskite. *Phys. Rev. B* **2018**, *97* (7), 075104. https://doi.org/10.1103/PhysRevB.97.075104.

(32) Shi, Y.; Xie, R.; Liu, X.; Zhang, N.; Aruta, C.; Yang, N. Tunable pH-Dependent Oxygen Evolution Activity of Strontium Cobaltite Thin Films for Electrochemical Water Splitting. *Phys. Chem. Chem. Phys.* **2019**, *21* (29), 16230–16239. https://doi.org/10.1039/C9CP02278C.

(33) Ichikawa, N.; Iwanowska, M.; Kawai, M.; Calers, C.; Paulus, W.; Shimakawa, Y. Reduction and Oxidation of SrCoO2.5 Thin Films at Low Temperatures. *Dalton Trans. Camb. Engl. 2003* **2012**, *41* (35), 10507–10510. https://doi.org/10.1039/c2dt30317e.

(34) Lu, N.; Zhang, P.; Zhang, Q.; Qiao, R.; He, Q.; Li, H.-B.; Wang, Y.; Guo, J.; Zhang, D.; Duan, Z.; Li, Z.; Wang, M.; Yang, S.; Yan, M.; Arenholz, E.; Zhou, S.; Yang, W.; Gu, L.; Nan, C.-W.; Wu, J.; Tokura, Y.; Yu, P. Electric-Field Control of Tri-State Phase Transformation with a Selective Dual-Ion Switch. *Nature* **2017**, *546* (7656), 124-128M. https://doi.org/10.1038/nature22389.

(35) Jeen, H.; Choi, W. S.; Biegalski, M. D.; Folkman, C. M.; Tung, I.-C.; Fong, D. D.; Freeland, J. W.; Shin, D.; Ohta, H.; Chisholm, M. F.; Lee, H. N. Reversible Redox Reactions in an Epitaxially Stabilized SrCoOx Oxygen Sponge. *Nat. Mater.* **2013**, *12* (11), 1057–1063. https://doi.org/10.1038/nmat3736.

(36) Hu, S.; Seidel, J. Oxygen Content Modulation by Nanoscale Chemical and Electrical Patterning in Epitaxial SrCoO3−δ ($0 < \delta \leq 0.5$) Thin Films. *Nanotechnology* **2016**, *27* (32), 325301. https://doi.org/10.1088/0957-4484/27/32/325301.

(37) Cui, B.; Werner, P.; Ma, T.; Zhong, X.; Wang, Z.; Taylor, J. M.; Zhuang, Y.; Parkin, S. S. P. Direct Imaging of Structural Changes Induced by Ionic Liquid Gating Leading to Engineered Three-Dimensional Meso-Structures. *Nat. Commun.* **2018**, *9*, 3055. https://doi.org/10.1038/s41467-018-05330-1.

(38) Gu, Y.; Xu, K.; Song, C.; Zhong, X.; Zhang, H.; Mao, H.; Saleem, M. S.; Sun, J.; Liu, W.; Zhang, Z.; Pan, F.; Zhu, J. Oxygen-Valve Formed in Cobaltite-Based Heterostructures by Ionic Liquid and Ferroelectric Dual-Gating. *ACS Appl. Mater. Interfaces* **2019**, *11* (21), 19584–19595. https://doi.org/10.1021/acsami.9b02442.

(39) Jeen, H.; Choi, W. S.; Freeland, J. W.; Ohta, H.; Jung, C. U.; Lee, H. N. Topotactic Phase Transformation of the Brownmillerite SrCoO2.5 to the Perovskite SrCoO3–δ. *Adv. Mater.* **2013**, *25* (27), 3651–3656. https://doi.org/10.1002/adma.201300531.

(40) Lu, Q.; Yildiz, B. Voltage-Controlled Topotactic Phase Transition in Thin-Film $SrCoO_x$ Monitored by In Situ X-Ray Diffraction. *Nano Lett.* **2016**, *16* (2), 1186–1193. https://doi.org/10.1021/acs.nanolett.5b04492.

(41) Kresse, G.; Joubert, D. From Ultrasoft Pseudopotentials to the Projector Augmented-Wave Method. *Phys. Rev. B* **1999**, *59* (3), 1758–1775. https://doi.org/10.1103/PhysRevB.59.1758.

(42) Kresse, G.; Furthmüller, J. Efficient Iterative Schemes for Ab Initio Total-Energy Calculations Using a Plane-Wave Basis Set. *Phys. Rev. B* **1996**, *54* (16), 11169–11186. https://doi.org/10.1103/PhysRevB.54.11169.

(43) Muñoz, A.; Calle, C.; Alonso, J.; Botta, P.; Pardo, V.; Baldomir, D.; Rivas, J. Crystallographic and Magnetic Structure of SrCoO2.5 Brownmillerite: Neutron Study Coupled with Band-Structure Calculations. *Phys. Rev. B - PHYS REV B* **2008**, *78*. https://doi.org/10.1103/PhysRevB.78.054404.

(44) Galakhov, V. R.; Kurmaev, E. Z.; Kuepper, K.; Neumann, M.; McLeod, J. A.; Moewes, A.; Leonidov, I. A.; Kozhevnikov, V. L. Valence Band Structure and X-Ray Spectra of Oxygen-Deficient Ferrites SrFeOx. *J. Phys. Chem. C* **2010**, *114* (11), 5154–5159. https://doi.org/10.1021/jp909091s.

(45) Lefler, B. M.; Postiglione, W. M.; Leighton, C.; May, S. J. Voltage Control of Patterned Metal/Insulator Properties in Oxide/Oxyfluoride Lateral Perovskite Heterostructures via Ion Gel Gating. *Adv. Funct. Mater.* **2022**, *32* (49), 2208434. https://doi.org/10.1002/adfm.202208434.

(46) D'Hondt, H.; Abakumov, A. M.; Hadermann, J.; Kalyuzhnaya, A. S.; Rozova, M. G.; Antipov, E. V.; Van Tendeloo, G. Tetrahedral Chain Order in the $Sr_2Fe_2O_5$ Brownmillerite. *Chem. Mater.* **2008**, *20* (22), 7188–7194. https://doi.org/10.1021/cm801723b.

(47) Young, J.; Rondinelli, J. M. Crystal Structure and Electronic Properties of Bulk and Thin Film Brownmillerite Oxides. *Phys. Rev. B* **2015**, *92* (17), 174111. https://doi.org/10.1103/PhysRevB.92.174111.

(48) Chestakov, D. A.; Parker, D. H.; Baklanov, A. V. Iron Monoxide Photodissociation. *J. Chem. Phys.* **2005**, *122* (8), 084302. https://doi.org/10.1063/1.1844271.

(49) Drechsler, G.; Boesl, U.; Bä\Smann, C.; Schlag, E. W. Mass Selected Anion-Zero Kinetic Energy Photoelectron Spectroscopy (Anion-ZEKE): Ground and Low Excited States of FeO. *J. Chem. Phys.* **1997**, *107* (7), 2284–2291. https://doi.org/10.1063/1.474622.

(50) Barnes, M.; Clouthier, D. J.; Hajigeorgiou, P. G.; Huang, G.; Kingston, C. T.; Merer, A. J.; Metha, G. F.; Peers, J. R. D.; Rixon, S. J. The Electronic Spectrum of Gaseous CoO in the Visible Region. *J. Mol. Spectrosc.* **1997**, *186* (2), 374–402. https://doi.org/10.1006/jmsp.1997.7456.

(51) Liu, F.; Li, F.-X.; Armentrout, P. B. Guided Ion-Beam Studies of the Reactions of Con+ (N=2–20) with O2: Cobalt Cluster-Oxide and -Dioxide Bond Energies. *J. Chem. Phys.* **2005**, *123* (6), 064304. https://doi.org/10.1063/1.1998836.

Table of Contents Artwork

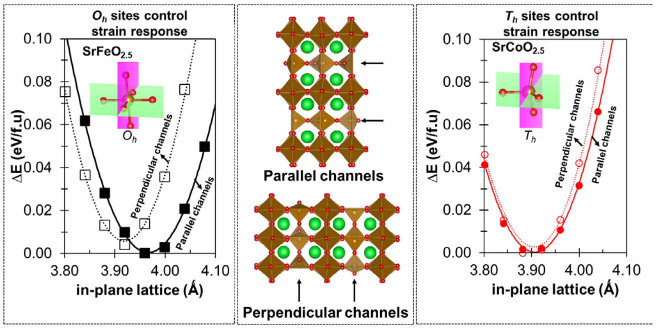

Supporting Information

Octahedral and tetrahedral coordination influences the ordering of oxygen vacancy channels in $SrCoO_{2.5}$ and $SrFeO_{2.5}$ thin films

Juan A. Santana,[1,2,3*] David Bugallo,[4] Andrew Mirea,[4] Tessa D. Tucker,[4] David Alfredo Gonzalez-Narvaez,[1] Alejandra Rosario-Crespo,[1] Yalexander Sanchez-Navarro,[1] Gabriela Marrero-Hernandez,[1,4] Kevin Rosa-Dieppa,[1,3] Andrea Garcia-Ramos,[1,3], Rajeev Kumar Rai,[5] Eric A. Stach,[5] Steven J. May,[4] Andrew M. Rappe[3]

[1]Department of Chemistry, University of Puerto Rico at Cayey, Cayey, PR 00737, USA
[2]Deanship of Academic Affairs, University of Puerto Rico at Cayey, Cayey, PR 00737, USA
[3] Department of Chemistry, University of Pennsylvania Philadelphia, Pennsylvania 19104-6323, USA
[4] Department of Materials Science and Engineering, Drexel University, Philadelphia, PA 19104, USA
[5]Department of Materials Science and Engineering, University of Pennsylvania, Pennsylvania 19104, USA

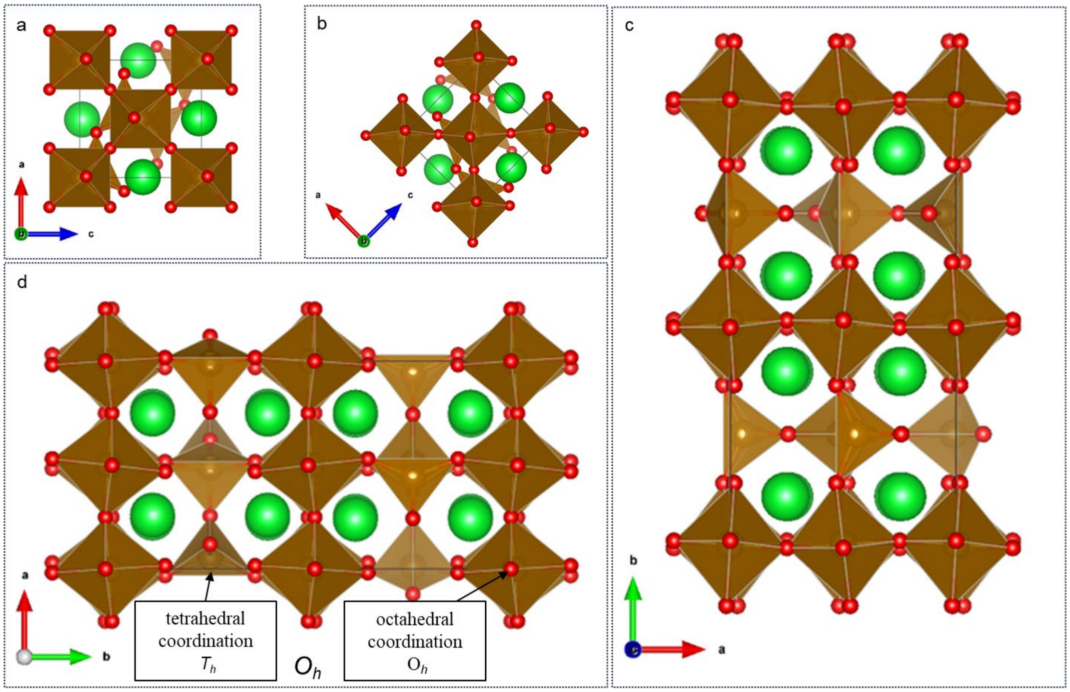

Figure S1. Sketch of the *Pnma* phase of brownmillerite with oxygen vacancy order (a, c) parallel and (b, d) perpendicular to a substrate. Panels c and d show the 72-atom simulation cell used in our DFT calculations, which is a 45° rotation of the cell in panel a.

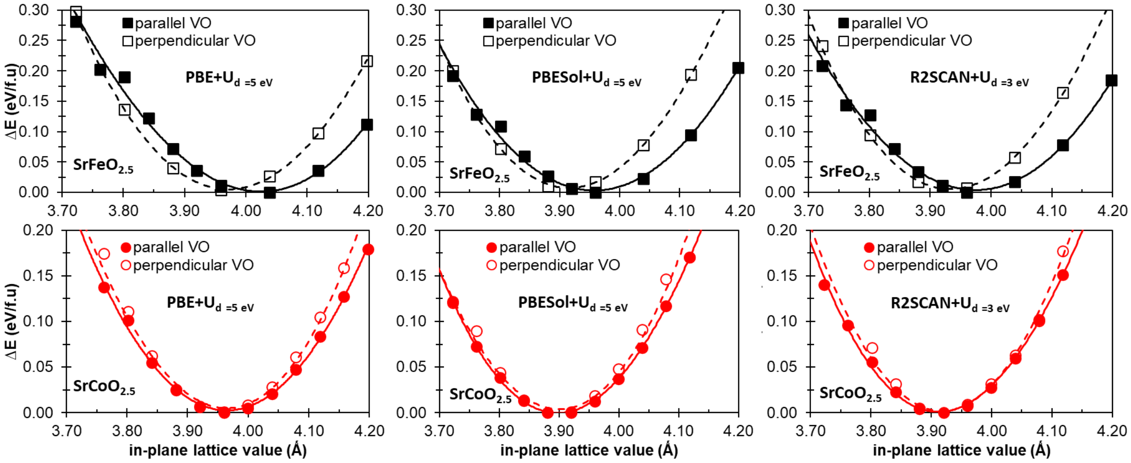

Figure S2: DFT calculated energy vs. imposed pseudocubic in-plane lattice parameter for unit cells of (upper panels) $SrFeO_{2.5}$ and (lower panels) $SrCoO_{2.5}$ with OVC in the (filled symbols) parallel and (empty symbols) perpendicular orientations. All calculations correspond to the AFM-G magnetic state. We can see that various DFT methods show a similar trend: different stable structures for each OVC ordering in $SrFeO_{2.5}$, but only one for $SrCoO_{2.5}$.

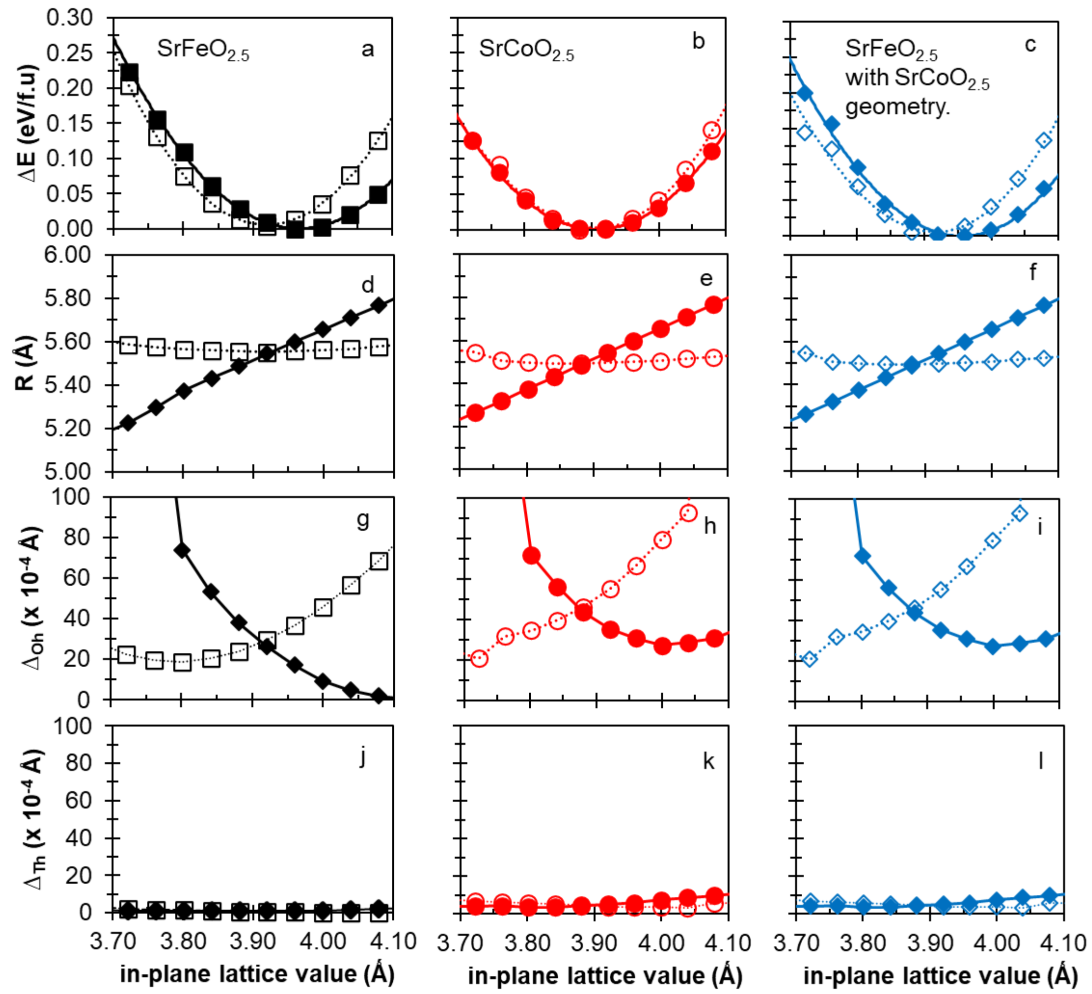

Figure S3: DFT calculated energy vs. imposed pseudocubic in-plane lattice parameter for unit cells of (a) $SrFeO_{2.5}$ and (b) $SrCoO_{2.5}$ with OVC in the (filled symbols) parallel and (empty symbols) perpendicular orientations. Panel c shows the results of single-point calculations for $SrFeO_{2.5}$ with the $SrCoO_{2.5}$ structure. Panels d, e, and f display the average chain separation R in the brownmillerite structure. Panels g, h, and i show the distortion Δ_{Oh} of the octahedra, and panels j, k and l the distortion Δ_{Th} of the tetrahedral. All calculations correspond to the AFM-G magnetic states. See below for the definition of Δ. The results suggest that electrostatic and elastic interactions are not the main drivers for the differences between $SrFeO_{2.5}$ and $SrCoO_{2.5}$.

Following Young and Rondinelli (*Phys. Rev. B* **2015**, *92* (17), 174111), we define the distortions Δ_{Oh} of the octahedra and Δ_{Th} of the tetrahedral using the averaged sum-of-squares difference between the calculated bond lengths (d_n) and the average bond length (d_{avg}):

$$\Delta = \frac{1}{N}\sum_{i=1}^{n}\left(\frac{d_n - d_{avg}}{d_{avg}}\right)^2$$